Type of paper: full-length article - revision (Journal Name: **International Journal of Heat and Mass Transfer. Code:** HMT-D-20-01180R2)
Date text revised: 12/2020
Number of words in the main text and tables = 6785
Number of figures = 14
Number of tables = 2

Predicting effective thermal conductivity in sand using an artificial neural network with multiscale microstructural parameters

Author 1
Wenbin Fei, PhD, ME, BE
Department of Infrastructure Engineering, The University of Melbourne, Parkville, Australia
ORCID: 0000-0002-9275-8403

Author 2
Guillermo A. Narsilio✉, PhD, MSc (Math), MSc (CE), CEng
Department of Infrastructure Engineering, The University of Melbourne, Parkville, Australia
ORCID: 0000-0003-1219-5661

Author 3
Mahdi M. Disfani, PhD, MSc, BSc
Department of Infrastructure Engineering, The University of Melbourne, Parkville, Australia
ORCID: 0000-0002-9231-8598

Full contact details of the corresponding author
Guillermo A. Narsilio, Deputy Head of Department (Research) & Associate Professor
Engineering Block B 208, Department of Infrastructure Engineering, The University of Melbourne, Parkville, VIC 3010, Australia
Email: narsilio@unimelb.edu.au, Phone: +61 (3) 8344 4659, Fax: +61 (3) 8344 4616

Abstract

Accurate and efficient prediction of thermal conductivity of sands is challenging due to the variations in particle size, shape, connectivity and mineral compositions, and external conditions. Artificial Neural Networks (ANN) models have been used to predict the effective thermal conductivity but they have not considered variables related to particle connectivity. This work uses computed tomography (CT) scanned images of four dry sands and network analysis to redress this significant shortcoming. Here sands are represented as networks of nodes (grains) and edges (interparticle contacts or/and small gaps between neighbouring particles) to extract network features that characterise interparticle connectivity. A network feature – *weighted coordination number* (WCN) capturing both particle connectivity and contact area – was found to be a good predictor of effective thermal conductivity in dry materials. Roundness, sphericity, solid particle thermal conductivity and porosity are other input parameters rigorously selected for an ANN model that predicts well the effective thermal conductivity of sands.

Keywords: Machine learning; Heat transfer; Thermal network model; Microstructure; Micro-CT.

1 Introduction

Granular materials are engaged in numerous applications such as geothermal engineering [1], petroleum and gas extraction [2], carbon dioxide geological storage [3] and pebble bed reactors [4]. In these projects, heat transfer is one of the processes that dominate project design and capital costs. As effective thermal conductivity (λ_{eff}) indicates the ease of heat transfer, its accurate and efficient prediction is essential. However, the prediction is challenging due to the complex microstructure of granular materials and external boundary conditions [5, 6]. The microstructure can be characterised at different scales, such as particle size, shape, gradation and minerality at the microscale (particle scale); particle connectivity [7, 8] at the mesoscale and porosity at the macroscale. Work by van Antwerpen et al. [9], Abdulagatova et al. [10] and Abyzov et al. [11] investigated a number of λ_{eff} models against experimental data and found some models simplify granular materials as packings of spheres, ellipsoids or parallel cylinders (regular geometrical forms), which limited their applicability to natural sands. Moreover, models characterise packing structure using porosity alone are insufficient [9] and microstructural parameters about grain-grain resistance [10] and contact area [11, 12] have not been incorporated in λ_{eff} models although they are important to λ_{eff} prediction [13]. In addition, particle connectivity, i.e., microstructural contact topology related to thermo-mechanical response [14], has rarely been quantified except for using coordination number which is defined as the number of neighbouring particles in contact with a given particle.

Recently, researchers abstracted granular materials as contact networks and thermal networks by creating nodes for particles and edges for interparticle contacts (contact networks), and with the addition of near-contacts which represent the small gaps between neighbouring particles (thermal networks) [15]. Then based on complex network theory [16], contact area or thermal conductance can be added as a weight to each edge in the network to eventually identify a single mesoscale network feature which can characterise both the particle connectivity and contact quality. One such feature from the contact network is the *weighted degree*, which represents an enhanced version of a coordination number that accounts for the contact area of each interparticle contact. Hence, while coordination numbers only count the number of neighbouring particles of a target particle, the weighted coordination number (WCN) quantifies both the contact number (particle connectivity) and contact area (contact quality). The physical meaning of the WCN is the total contact area of a target particle to its neighbours.

Numerical simulation methods such as finite element methods (FEM) [17], discrete element methods (DEM) [18] and lattice Boltzmann methods (LBM) [19] can be used to estimate λ_{eff}

with a more detailed complex microstructure involved in the process. However, these approaches require solving a system of partial differential equations and the computations are generally time-consuming [14, 20]. On the other hand, physical experiments such as thermal needle probe test are commonly undertaken to measure λ_{eff} [21], but one of the drawbacks is that accurate measurement needs relatively large undisturbed samples (150 mm long, 50 mm in diameter as a minimum) which may be difficult to obtain. The aim of this paper is to develop a model that can predict λ_{eff} accurately and computationally efficiently, even from very small samples.

Machine learning techniques have enabled substantial advances in data-driven approaches throughout academia and industry. In the material sciences, materials informatics combine machine learning, Bayesian optimisation and Monte Carlo tree searches in an attempt to address the challenge of rapidly finding optimal materials [22]. A limited number of studies have also used machine learning to predict λ_{eff} of sphere packings [14, 23], equation-based irregular materials [20] and sands [24]. The input parameters for the machine learning models in these works include porosity, particle size, component content, the thermal conductivity of solid and interstitial gas, temperature and loadings. Although these parameters are measurable in a laboratory [25, 26], bypassing a detailed understanding of structural arrangements and physical mechanisms may result in the differences observed between calculations and measurements [9, 13]. Hence, it is necessary to include particle connectivity parameters and the variables detailed above, in machine learning models that investigate heat transfer.

This work intends to predict λ_{eff} accurately and efficiently by developing an ANN model using important and non-redundant inputs. Here we justify the selection of average WCN (WCN_{ave}) which quantifies the topological structure in sands and other microstructural variables including particle diameter, three-dimensional sphericity and roundness as input parameters in the ANN model. Computed tomography (CT) scanned images of four dry sands that varied in shape, size and endured external loads are used to calculate these parameters. A recently developed in-house thermal conductance model (TCNM) computed the λ_{eff} acting as the output parameter in the ANN model [27, 28] alongside complementary experimental measurements. TCNM mitigates the overestimation of λ_{eff} possibly induced by the particle volume effect [29] from threshold segmentation, and the variations of λ_{eff} estimation for different particle arrangements without additional disturbance of samples that result from insertion of thermal probes.

2 Artificial neural network models

Artificial neural network (ANN) is at the core of deep Machine Learning (ML) techniques and has managed to render high accuracy in image classification (e.g., Google Images), voice recognition (e.g., Apple's Siri) and learning (e.g., AlphaGo). The ANN was inspired by the architecture of the human brain and its architecture composites of an input layer, one or more hidden layers and an output layer. Each layer has one or more neurons (units/nodes), with the neurons in different layers connected by edges. As this work attempts to find an accurate and efficient model to predict λ_{eff}, the neurons in the input layer could be microstructural variables while the neuron in the output layer is λ_{eff}. Non-linear functions (activation functions) with weights that correspond to the neurons in the previous layer compute the neurons in the latter layer. This paper employs the ReLU activation function embedded in Python library TensorFlow and Keras for the hidden layers due to its high efficiency and general applicability [30]. In addition to the selection of a robust activation function, an appropriate optimiser can also adjust the weights and learning rates. This work uses Adam optimisation because it is an adaptive learning rate algorithm and has several advantages of other optimisation algorithms such as Momentum optimisation and RMSProp [30].

2.1 Input parameters determination

Even though ANN performs well in solving complex problems, feeding input features without discretion is not recommended. Sometimes, a larger number of input features might lead to overfitting, making the trained model only fit specific data [31]. Hence, feature selection and reduction are usually conducted to find the most relevant and least redundant input features before training a machine learning model. This section presents a review of the heat transfer mechanisms and λ_{eff} models to justify the inputs selected in this work.

Heat transfer in gas-stagnant granular materials occurs via four critical pathways: (1) heat conduction within solid particles; (2) heat conduction via interparticle contacts; (3) heat conduction via particle-gas-particle; (4) heat radiation across the solid surface and is negligible when the temperature is below 600° [10]. Since the thermal conductivity of the solid is two orders of magnitude larger than air and this work focuses on the samples at room temperature, heat travels via the first two mechanisms is known to be more significant for dry soils [32]. Therefore, the ANN model in this work incorporates parameters that relate to the particle and interparticle contacts. Particle diameter should be an input parameter since it relates to the distance that heat transfers within the particles, so is the solid thermal conductivity controlling the ease of heat transfer in the particle. In terms of a parameter related to interparticle contact, the WCN_{ave} was identified as a good candidate [15] due to its capacity to capture both the existence of interparticle contacts but also the area of contact.

Selection of optimal input parameters for the ANN model involved a critical analysis of the existing parameter used in λ_{eff} models. The majority of λ_{eff} models use porosity and the thermal conductivity of different phases [9-11]. Some complex λ_{eff} models in Table 1 also consider particle/pore shape which affects heat transfer [33] and mechanical behaviour [34] of granular materials. Eq. (1) introduces a parameter B to adjust the particle shape while Eq. (2) and Eq. (3) employ an aspect ratio to characterise the shape of the particle and/or pore. However, these are only applicable to particles with regular shapes.

Table 1 Summary of effective thermal conductivity models that consider particle/pore shape

Reference		
Zehner and Schlunder [35]	$\frac{\lambda_{eff}}{\lambda_f} = 1 - \sqrt{1-\phi} + \frac{2\sqrt{1-\phi}}{1-\xi B}\left[\frac{(1-\xi)B}{(1-\xi B)^2}\ln\left(\frac{1}{\xi B}\right) - \frac{B+1}{2} - \frac{B-1}{1-\xi B}\right],$ $\xi = \frac{\lambda_f}{\lambda_s},\ r^2 + \frac{z^2}{[B-(B-1)z]^2} = 1.$ r and z are the radii of the particle in two principal axes. B is the shape factor. The particle becomes the z-axis with no solid volume when $B \to 0$, a sphere when $B \to 1$ and a cylinder when $B \to \infty$.	(1)
Fricke [36]	$\frac{\lambda_{eff}}{\lambda_s} = \frac{(1-\phi)(1-\xi)+\xi\beta\phi}{(1-\phi)(1-\xi)+\beta\phi},\ \xi = \frac{\lambda_f}{\lambda_s},$ β is related to ξ and aspect ratio.	(2)
Keller et al. **[37]**	$\lambda_{eff} = \lambda_s\left[1 + \frac{\alpha_p}{\alpha_s}\left(\frac{b}{a}\right)^2\left(2 - \frac{b/a}{(1-b/a)^2}\right)\right]^{-1},\ \phi = \frac{\alpha_p}{\alpha_s}\left(\frac{b}{a}\right)^2\left(2 - \frac{b}{a}\right),$ α_p is the aspect ratio of the pore α_s is the aspect ratio of solid (grain) b is the pore radius while a is the grain radius.	(3)

λ_s is the thermal conductivity of solid and λ_f is the thermal conductivity of gas/fluid in the void space, ϕ is porosity.

Since aspect ratio cannot adequately cover the shape of all irregular particle/pores [33], three-dimensional (3D) sphericity (S in Eq. (4)) and roundness (R in Eq. (5)) were used in this work to describe the particle shape, details of computational steps can be found in [33]:

$$S = \frac{36\pi V^2}{\mathrm{SA}^3} \tag{4}$$

$$R = \frac{\sum r_i/N}{r_{max-in}} \tag{5}$$

where V is particle volume, SA is particle surface area, r_i is the radius of each corner [33], N is the total number of corners and r_{max-in} is the radius of the largest sphere in the particle.

Selection of particle size, the thermal conductivity of solid and fluid/gas, WCN_{ave}, 3D sphericity and roundness, and porosity as sensible candidates for input parameters in the ANN model considered the analysis above.

2.2 Performance indicator

Data used for ANN modelling is typically divided into three sets: a training set, a validation set and a test set when embarking in supervised ML. The training set first trains the ML models which are evaluated to select the one that has the best performance on the validation set. The test set then evaluates the performance of the final model.

Quantifications of the evaluations can use either the mean square error (MSE) or correlation coefficient (R^2). MSE measures the *standard deviation* of the errors that a model makes in its predictions, with the preferred application [30] for regression problems. In contrast, R^2 usually quantifies the linear correlation between the predicted value and actual value. It has a range from 0 to 1, where 0 signifies no relationship while 1 indicates a perfect fit. Accordingly, MSE was employed in this study to monitor the performance of the ANN model when tuning hyperparameters (e.g., the number of nodes in each layer) to select models with R^2 used to present the general performance of the ANN model.

3 Data collection

3.1 Materials

Four sands varying in particle shape were sent to the Australian Synchrotron, Imaging and Medical BeamLine (IMBL) for CT scanning at a pixel size of 13 μm. Figure 1 shows a selection of the acquired images. Glass beads display the roundest particles while the particles in the Ottawa sand are more irregular but still have round corners. Compared to the particles in the Ottawa sand, particles in the angular sand are even more irregular and have sharp corners. Lastly, particles made from crushing schist have the most irregular shape, with half of these platy and elongated.

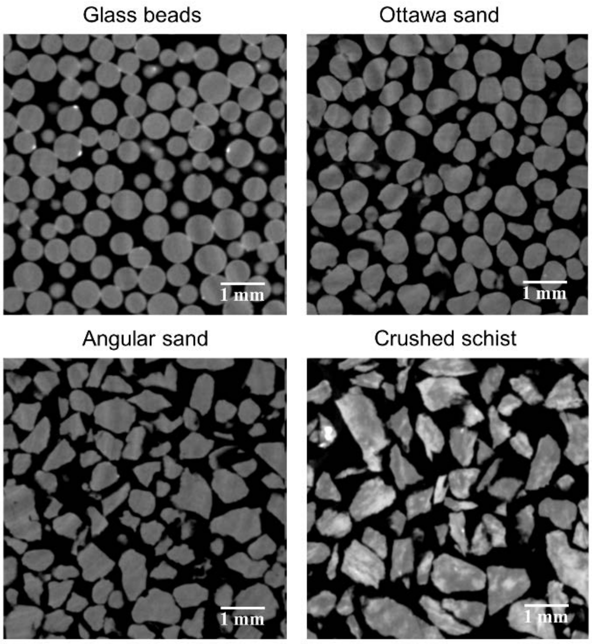

Fig. 1. Selected micro-CT slide images of four sands. Images show the variations in particle shape.

Different particle sizes were chosen and axial loads were applied to sands in Fig. 1 using a rigid wall cell to further vary porosity and particle arrangement (Table 2). Hence, more data were obtained to train a universal ANN. Calculations of the equivalent particle size used CT images, consistent with previous research [27]. The samples shown in Fig. 1 correspond to GB-L, OS, AS-L and CS-M without axial stress in Table 2 and have similar equivalent D_{50}.

Table 2 Particle size and axial compression stresses applied to each sample

Sand	Sample name	Particle size (mm)[a]	Particle size (mm)[b]	Equivalent D_{50} (mm)[b]	Axial Stress (MPa)
Glass beads	GB-S	0.20-0.30	0.12-0.37	0.24	0, 2.0, 6.1, 10.2
	GB-N	0.50	0.33-0.68	0.54	0, 2.0, 6.1, 10.2
	GB-L	**0.50-0.70**	**0.40-0.80**	**0.60**	**0, 2.0, 6.1, 10.2**, 20.4, 40.7
Ottawa sand	**OS**	**0.60-0.85**	**0.58-0.94**	**0.76**	**0, 2.0, 6.1, 10.2**, 20.4, 40.7
Angular sand	AS-P	0.15-0.30	0.12-0.41	0.24	0
	AS-M	0.43-0.60	0.32-0.64	0.48	0, 2.0, 6.1, 10.2, 20.4, 40.7
	AS-L	**0.60-1.18**	**0.39-0.99**	**0.68**	**0, 2.0, 6.1, 10.2**, 20.4, 40.7
Crushed schist	CS-S	0.30-0.50	0.17-0.61	0.39	0, 2.0, 6.1, 10.2
	CS-M	0.50-1.18	0.23-0.95	0.58	0

[a] Particle size from sieve analysis

[b] Particle size calculated based on CT reconstructed sample.

3.2 *Microstructural variables*

This section briefly introduces the procedure used to obtain the aforementioned particle size, WCN, 3D sphericity, 3D roundness and porosity.

3.2.1 *Image processing*

The CT scanning resulted in sequential images with a pixel size of 13 μm. Selection of four regions of interest (ROI) with a dimension of $4.55 \times 4.55 \times 4.55$ *mm* in each image stack eliminated the effect of potential heterogeneity. Fig. 2 (a) shows a cross-section of the ROI after applying a 3D median filter. Then a commonly used Otsu threshold segmentation algorithm [38] distinguished the solid phase (in black) and air phase (in white) as shown in Fig. 2 (b). The adjacent particles in Fig. 2 (b) remain connected and required 'splitting' to achieve the properties (i.e., particle size, shape and WCN) of each particle using watershed segmentation. Meanwhile, each particle was assigned a unique identifier (ID) and rendered by random colour as shown in Fig. 2 (c). The Taubin smooth algorithm smoothed out each particle surface to compute particle volume, particle surface area, 3D sphericity and roundness following the steps detailed in a recent work [33]. Equivalent particle size calculations used the particle volume, with porosity computed using the volumes of all the particles and the known dimension of the ROI.

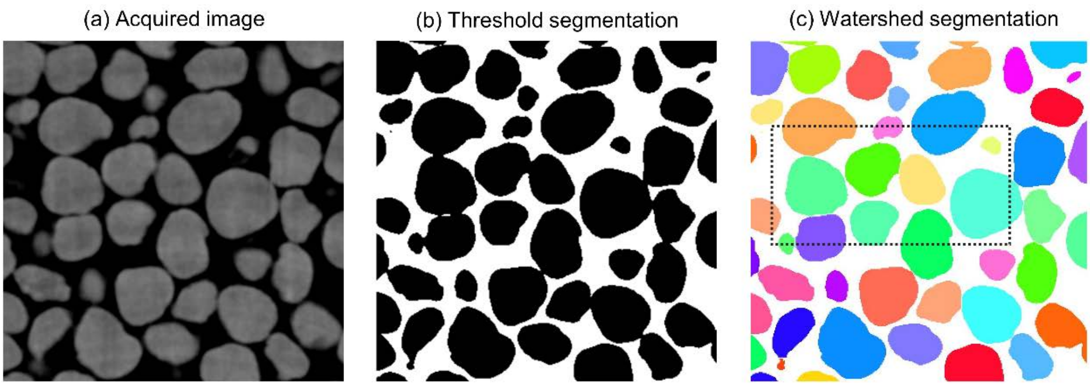

Fig. 2. Overview of key steps in image processing to identify individual particles

3.2.2 *Weighted coordination number (WCN)*

Classical coordination number quantifies the contact number of a particle, a weighted coordination number (WCN) weights each interparticle contact by the contact area. Hence, WCN can capture both the existence of contacts and contact area. WCN is termed weighted degree in complex network theory [16] and can be computed after network constructions. For each sample in this work, a contact network was constructed by creating a node at the centroid of each particle and an edge for each interparticle contact, as shown in Fig. 3. To identify the interparticle contacts, boundary voxels were recognised first if the voxels in a particle are adjacent to anything else that was not in the same particle. The average coordinate of the boundary voxels can help to locate the centroid of each particle. Furthermore, if boundary voxels bordered on another particle, these were identified as interparticle contact voxels and further used to estimate the interparticle contact area.

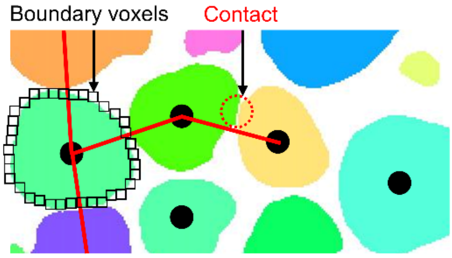

Fig. 3. Contact network construction for a sample (detailed from the dashed rectangle in Fig. 2 (c))

A simple way to calculate the interparticle contact area is to directly count the number of interparticle contact voxels but this may result in an overestimation after threshold segmentation due to partial volume effects [29]. Each pixel in the CT image shown in Fig. 4 (a) has its own grayscale. Black and white voxels indicate solids and voids, whereas other voxels are "grey". Some of these grey voxels at the 1-pixel gap between the two particles (Fig. 4 (a)) are incorrectly identified as contacts, which will result in overestimations of both the contact area and λ_{eff}.

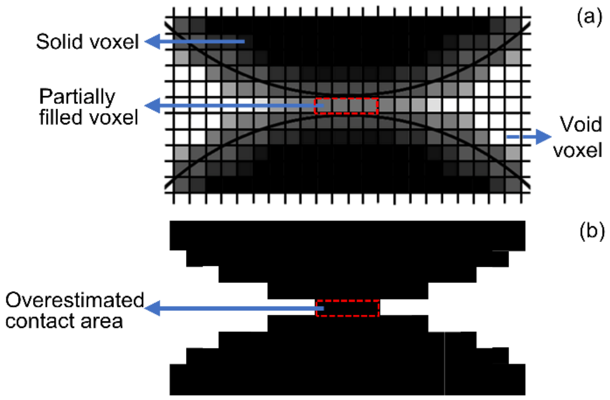

Fig. 4. CT image of two spheres with a voxel gap. This image displays some partially filled voxels (a) incorrectly identified as contact areas after (b) threshold segmentation.

To correct the interparticle contact area, a penalty factor considering the grayscale of these partially filled voxels was introduced. The corrected interparticle contact area A^C was computed as the sum of $A^v_{(i,j,k)}$ weighed by the τ^{th} power of the ratio of grayscale values of individual interparticle voxels $g_{(i,j,k)}$ to the maximum grayscale value among all interparticle voxels (Eq. (6)). The penalty factor τ was set at 10 after the calibration of the λ_{eff} of sphere packings with the result from a theoretical thermal network model [28, 39]:

$$A^C = \sum_{i,j,k} A^v_{i,j,k} = \sum_{i,j,k} \left[\left(\frac{g_{(i,j,k)}}{\max[g_{(i,j,k)}]} \right)^{\tau} L_v^2 \right] \tag{6}$$

where L_v is the length of a voxel, which is 13 μm in this work.

Once the contact network was constructed and interparticle contact area calculated, a computationally efficient Python library *graph-tool* [40] calculated the WCN (i.e., *degree* in the terminology of complex network theory with the addition of the interparticle contact area to each corresponding edge). The degree of a node is the total number of its attached edges, whereas the weighted degree of a node is equal to the sum of weights at the attached edges [16].

3.3 *Effective thermal conductivity estimations*

3.3.1 *Effective thermal conductivity from thermal conductance network model (TCNM)*

In order to calculate λ_{eff}, the contact network in Fig. 3 can be extended to a thermal network by considering the small gaps as near-contacts (i.e., the blue edges in Fig. 5), which correspond to particle-gas-particle heat conduction. A near-contact was identified if the distance between the boundary voxels of two adjacent particles was shorter than the average particle radius [27, 28]. Then a TCNM model was generated by calculating the thermal conductance at three main heat transfer paths (i.e., through the particles, interparticle contacts and near-contacts), which is valid for dry granular materials at room temperature.

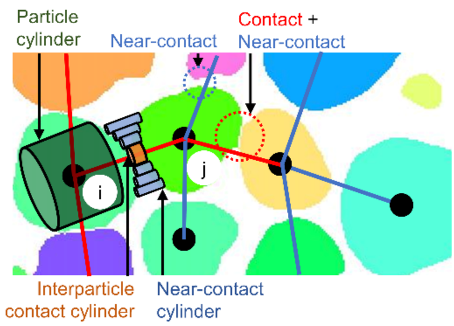

Fig. 5. Thermal network construction. Red edges represent interparticle contacts while blue edges indicate near-contacts. An equivalent particle cylinder (dark green), an interparticle contact cylinder (orange) and a series of near-contact cylinders (light blue) are used to calculate thermal conductance

through the particle, interparticle contact and near-contact. The process is repeated for all particles within the granular material.

Figure 5 presents three types of equivalent material cylinders that correspond to the three heat transfer mechanisms and are used to calculate the thermal conductance. The thermal conductance C_{cy} of a cylinder with a thermal conductivity λ_{cy}, cross-section area A^{cy} and length L^{cy} is computed as $C_{cy} = \lambda_{cy} A^{cy}/L^{cy}$. Hence, the thermal conductance C^P through an equivalent particle cylinder (the dark green cylinder in Fig. 5) was calculated as the following:

$$C^p = \lambda_s \frac{A^p}{L^p} = \lambda_s \frac{V^P/L^P/CN}{L^P} \tag{7}$$

where λ_s is solid thermal conductivity, A^P is the cross-section area of the green cylinder, V^P is the particle volume, L^P the distance from the particle centroid to the corresponding contact and CN is the coordination number of the target particle.

Similarly, calculations of thermal conductance $C^{contact}$ used Eq. (8) via an interparticle contact cylinder (orange cylinder in Fig. 5) with the corrected interparticle contact area A^C obtained from Eq. (6). The length of the contact cylinder was defined as $3L^v$ (L^v *is the pixel size or voxel length*) as suggested by [41] which was a validation of [42]. A coefficient κ was also introduced in Eq. (8) to indicate the particle surface roughness since interparticle contact is a combination of point-to-point contacts in real due to the surfaces roughness but are not presented in CT images in Fig. 1 due to the physical limitation of the CT facility. κ was set as 0.75 since Askari et al. [43] concluded that the overestimation of the interparticle contact area might be 25% if neglecting the effect of roughness.

$$C^{contact} = \lambda_s \frac{\kappa A^C}{3L^v} \tag{8}$$

The thermal conductance C^{gap} through the near-contacts is the sum of the thermal conductance C^g (Eq. (9)) via each near-contact cylinder (light blue in Fig. 5). The cross-section area of the cylinder is the area of a pixel ($(L^v)^2$) with the length of the cylinder computed during the identification process.

$$\mathrm{C}^{gap} = \sum_l C_l^g = \lambda_v (L^v)^2 \sum_l \frac{1}{L_l^g} \tag{9}$$

The three conductance are combined to calculate the equivalent capacitance C_{ij} between the centroid of particle i and j using Eq. (10). The $C^{contact}$ is zero when two adjacent particles that only have a near-contact (small gap).

$$C_{ij} = \left[\frac{1}{C_i^p} + \frac{1}{(C^{contact} + C^{gap})} + \frac{1}{C_j^p}\right]^{-1} \tag{10}$$

The calculated C_{ij} using Eq. (10) was imported to Eq. (11)(the Fourier's law) to calculate heat flux Q_{ij} using an open-source Python library, OpenPNM [44] as a function of the temperature T in nodes i and j:

$$\sum_{i \to j} Q_{ij} = \sum_{i \to j} C_{ij}(T_i - T_j) \tag{11}$$

The temperatures on the opposite sides of the sample (inlet and outlet) were prescribed as T_{in} = 293 K and T_{out} = 292 K to create a small thermal gradient, with other boundaries simulated as in thermally isolated conditions (or symmetrical, Q_{ij} = nil on these boundaries). The Q_{ij}, integrated on a cross-section perpendicular to the dominant heat transfer direction was selected to calculate the λ_{eff} of the sample as:

$$ETC = \frac{\frac{1}{A}\sum Q_{ij}}{(T_{in} - T_{out})/L} \tag{12}$$

where A is the area of a selected cross-section, L is the length of the simulated sample.

Since the penalised interparticle contact area from Eq. (6) and a coefficient related to particle surface roughness were used in Eq. (8) to calculate the thermal conductance at interparticle contacts, TCNM has the merit of mitigating the overestimation of λ_{eff} caused by the partial volume effect and particle surface roughness.

3.3.2 Effective thermal conductivity from physical testing

The selected sand samples were also poured into PVC containers with a height of 120 mm and diameter of 50 mm using the same air-pluviation method to ensure consistency with the samples used in CT scanning. A thermal needle probe with a length of 100 mm and diameter of 2.4 mm was used to measure the λ_{eff} of each specimen following the ASTM standard D5334-14 [21]. The PVC containers, whose size satisfy the requirement in ASTM standard, were also scanned to check density consistency with the smaller axially loaded micro-CT scanned samples.

4 Results and discussion

In this section, the TCNM is first validated for computing effective thermal conductivity λ_{eff} followed by a comprehensive discussion for selecting the important and non-redundant input parameters for the ANN models. Since WCN_{ave} is a newly introduced mesoscale parameter, the potential benefits of its inclusion in the prediction of λ_{eff} is investigated. Additionally, the relationships between WCN_{ave}/ WCN and traditional parameters are analysed for feature reduction.

4.1 Effective thermal conductivity results and TCNM validation

From the CT images of each sand under no load, four small cubic ROIs with an edge length of 4.55 *mm* were selected by cropping the CT images at different locations. The subsamples are used for λ_{eff} and porosity calculations in TCNM and comparisons with physical testing. Although the different grayscales in the CT images in Fig. 1 indicate minerals with different densities and thermal conductivities in the sands, a fixed thermal conductivity (3 W/(mK)) previously used in papers [39, 45] was assigned to solids to eliminate the effect of mineral composition, and isolate the effects of microstructures such as particle shape, connectivity and porosity. The thermal conductivity of air was set as 0.025 W/(mK). Figure 6 illustrates that the λ_{eff} from the TCNM have a similar decreasing trend to the experimental results. The λ_{eff} using the two methods are close for Ottawa sand (OS) while the λ_{eff} from TCNM is larger than measurements for angular sand (AS-L) and crushed schist (CS-M). The main reason is that the thermal conductivity of the solid phase in all samples are set same in TCNM simulation but different in reality.

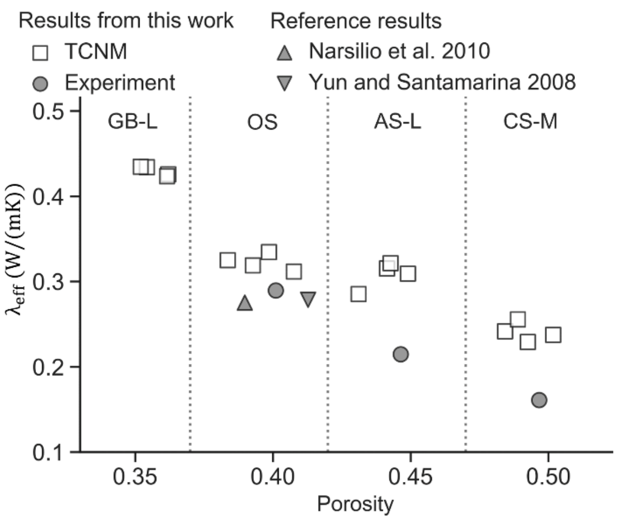

Fig. 6. The effective thermal conductivity computed from TCNM and validated by the experimental results of glass beads (GB-L), Ottawa sand (OS), angular sand (AS-L) and crushed schist sand (CS-M).

4.2 *Effect of WCN_{ave} on effective thermal conductivity*

The thermo-mechanical behaviour of granular materials under loads not only relates to the bulk properties such as porosity but also microstructural contact variables [14] such as the WCN_{ave}. Therefore, the effect of WCN_{ave} on λ_{eff} should be investigated. For GB-L, OS and AS-L under stress levels of 0, 2, 6.1 and 10.2 MPa, the average λ_{eff} of the four subsamples in each sand were calculated. Fig. 7 (a) shows that their average λ_{eff} has a directly proportional relationship with the WCN_{ave}, in contrast to the inverse proportionality with porosity (Fig. 7 (b)). The data from GB-L and OS in Fig. 7 (a) align along an overall trendline while the data in Fig. 7 (b) cluster in three groups. Since particles in the three sands have distinct shapes, Fig. 7 (a) and Fig. 7 (b) were extended to include an additional dimension, by considering the average of sphericity and roundness in the third axis. Planes were also fitted to the data with calculated R^2 in the 3D graphs shown in Fig. 7. Fig. 7 (c) shows that the R^2 is high at 0.98, which indicates that the microscale geometrical parameters together with mesoscale topographic and contact quality variable can predict λ_{eff} well. If the macroscale porosity replaces the mesoscale WCN_{ave} as shown in Fig. 7 (d), the R^2 decreases to 0.88, which suggests that porosity alone cannot characterise the microstructure. This also highlights the importance of mesoscale connectivity parameters in studies of sand thermo-mechanical responses.

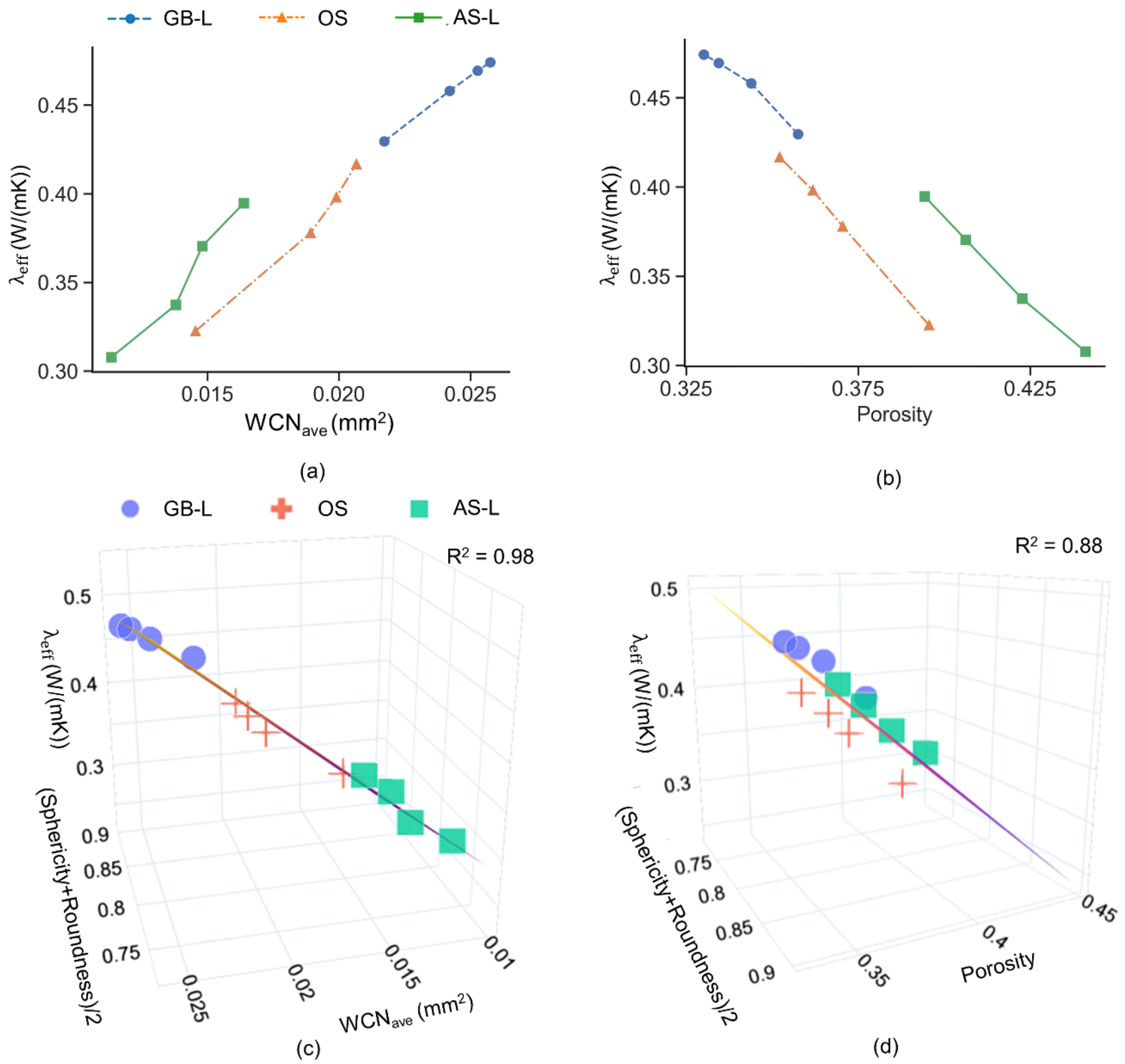

Fig. 7. The relationship between effective thermal conductivity and (a) WCN_{ave}, (b) porosity, (c) WCN_{ave} and particle shape, and (d) porosity and particle shape. (Click here to access the interactive graphs).

4.3 Relationships between WCN_{ave}/ WCN and traditional parameters

This section presents an analysis of why the WCN_{ave} can be an λ_{eff} predictor. From the perspective of complex network theory, the WCN_{ave} unifies the coordination number (connectivity) and contact area (as a weight in each edge of the network) as a single parameter. While the axial stress under zero lateral strain on samples is *under 2 MPa*, Fig. 8 shows that the slopes of the correlation between axial stress and λ_{eff} (Fig. 8 (a)) are similar to the slopes of the relationship between axial stress and contact area for three soils (Fig. 8 (c)). The WCN_{ave} also has similar corresponding increasing slopes (Fig. 8 (b)). Although the coordination number versus axial stress trends also increase, the gradients for OS and AS-L (for axial stress ≤ 2MPa) are different from the corresponding gradients observed in effective thermal conductivity versus axial stress. The contact area shows a stagnant increase as the axial stress increases beyond 2 MPa, (Fig. 8 (c)) which is no longer the same as the gradients observed in the λ_{eff} plots (Fig. 8 (a)). However, coordination numbers and the WCN_{ave} can capture the increase of λ_{eff} when the axial stress is larger than 2 MPa. In other words, the WCN_{ave} can closely follow the increase of λ_{eff} over the whole range of axial stress since it captures the advantages of both contact area and coordination number at different stages of axial stress. Fig. 8 (b) also shows that the WCN_{ave} has a good relationship with axial stress for each sand and the value in spherical GB-L is always the highest, which indicates that stress may be redundant and may not be necessary for the ANN model to predict λ_{eff} if WCN_{ave} is used.

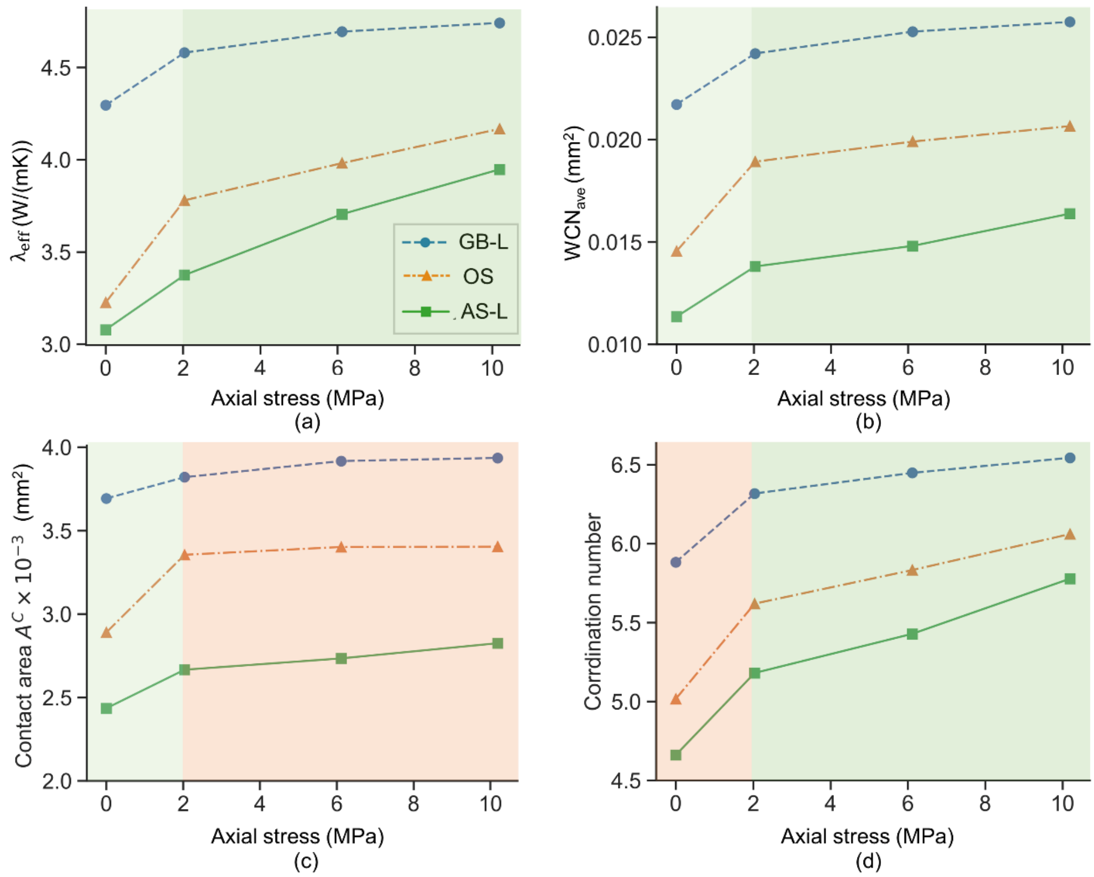

Fig. 8. Variation of (a) effective thermal conductivity, (b) WCN_{ave} , (c) average intercontact area and (d) average coordination number with axial stress (and zero lateral strain).

As one of the main heat transfer processes is through particles in dry granular materials, the particle diameter affects the heat transfer distance in the particle and the impact on WCN should be explored. For GB-L, OS and AS-L under no load, particles in the four ROIs of each sand (4,898 individual particles from 12 ROIs in total) were used to investigate the relationship between the equivalent particle diameter and WCN. A clear and directly proportional relationship between particle equivalent diameter and WCN can be seen in Fig. 9 (a) for spherical GB-L, which is reasonable since a large particle has a higher opportunity to touch more particles and a larger total contact area once touching. The positive trend also exists in Fig. 9 (b) and Fig. 9 (c) for more irregular OS and AS-L sands even though there is a divergence in Fig. 9 (c). Therefore, the equivalent particle diameter is unnecessary to be involved in the ANN model on top of the WCN for λ_{eff} prediction due to their intercorrelation.

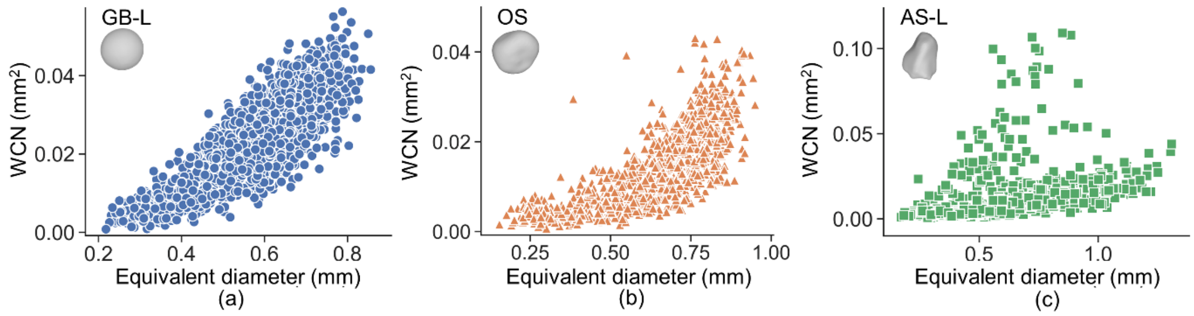

Fig. 9. The dependence of WCN on equivalent particle diameter for three selected sands

4.4 *Effect of WCN on heat flux*

Since heat flux was used in Eq. (11) to compute λ_{eff}, the particles at the inlet and outlet of a subsample in each sand were used to study the relationship between WCN and heat flux. The heat flux from the centroid of a particle to the centroid of all its neighbours was calculated in the TCNM, showing positive correlations to WCN displayed in Fig 10. The clear relationship is because the WCN considers contact area which was used to calculate thermal conductance (Eq. (8)) and further served the computation of heat flux using the Fourier's law. Similar to Figure 9, the correlation is clearest in the spherical GB-L and becomes weaker in more irregular sands.

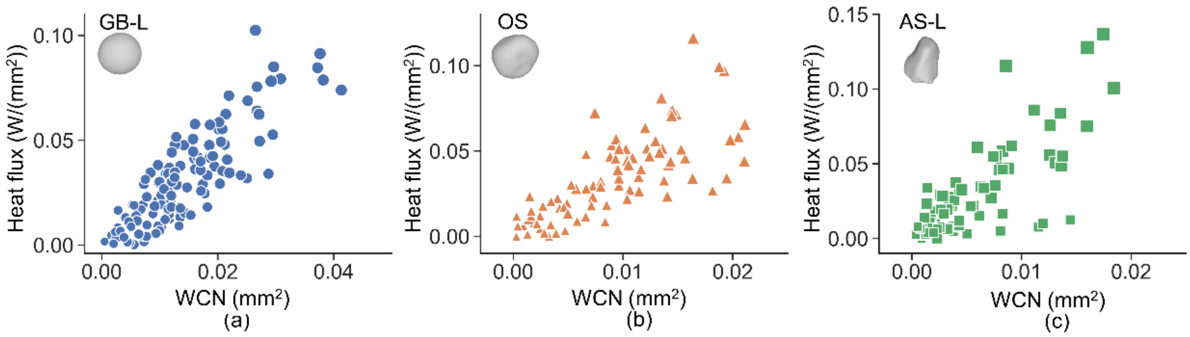

Fig. 10. The relationship between the total heat flux and WCN of particles at inlet and outlet in three selected sands

4.5 ANN model construction

Only a small subset of all samples was used in the above analyses (those shown in bold in Table 2). Data from more samples are required to construct an ANN model. Four subsamples (ROIs) from all 152 samples in Table 2 were selected and the solid material of each particle in each ROI was assigned three different thermal conductivities, to render 456 datapoints used for the ANN model. The average 3D sphericity, 3D roundness, WCN_{ave}, porosity and λ_{eff} under a larger range of loads (up to 40.7 MPa) for these samples were calculated. In addition to setting the thermal conductivity of the solid phase as 3 W/(mK), 5 and 7 W/(mK) were also used for enriching the database. Although dimensionless $\lambda_{eff}/\lambda_{solid}$ instead of λ_{eff} was used as the output of the ANN model, the data in Fig. 11 (a) whose markers were rendered by λ_{solid} still shows three distinct cluster groups that correspond to different λ_{solid}. Therefore, the ANN model also requires λ_{solid} as an input parameter. The markers in Fig. 11 (a) represent different sands and the size of the markers indicates the equivalent average particle diameter of the subsample. Figure 11 (b) presents the same data as Fig. 11 (a) but the markers show the loadings applied to the subsamples. The data were randomly split into a training set (80%), validation set (10%) and a testing set (10%).

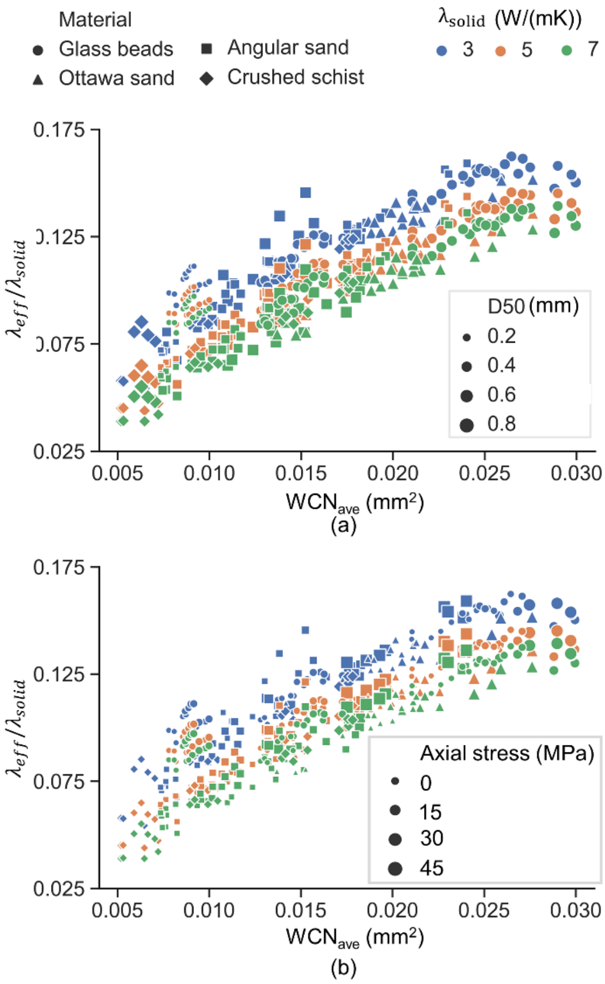

Fig. 11. The database used to construct the ANN model.

4.5.1 *ANN model I: λ_{solid}, sphericity, roundness and WCN_{ave} as input parameters*

Packing structure models [46] are a type of models that use particle topology to predict λ_{eff}. However, few studies have been conducted except measuring particle connectivity using Voronoi tessellation [47], typical lattice structure [48] or bond orientation [49]. Since the WCN_{ave} can quantify the structure of granular materials, ANN model I used λ_{solid}, sphericity, roundness and the WCN_{ave} (but not porosity) as input parameters and $\lambda_{eff}/\lambda_{solid}$ as the output to imitate the *packing structure models* [46]. Figure 12 shows that sphericity and roundness display a good correlation to each other with R^2 of 0.96 for the four tested sands. Still, complete coverage of the wide range of irregular particle shapes requires both parameters, as shown in [33]. The R^2 of the correlation between each pair of the particle shape descriptors, WCN_{ave} and λ_{solid} in Fig. 12 are not high, which implies that these input parameters are not redundant for ANN model I. The R^2 of the relationship between WCN_{ave} and $\lambda_{eff}/\lambda_{solid}$ is 0.87, and indicates that interparticle connectivity and contact quality play crucial roles in the heat transfer of dry granular materials.

Fig. 12. A heatmap presents the R^2 between each pair of features used in ANN model I

The ANN is suitable for numerous complex problems due to its flexibility, which is also one of its main drawbacks [30]. Values of model and algorithm parameters (i.e., hyperparameters) should be decided since any imaginable network topologies can be used. This study tuned the learning rate η, the neuron number in the hidden layer, and the structure indicating how neurons are interconnected to find the desirable ANN model. MSE was used to monitor the error during the training processes until *epoch* reached 2,000. An epoch is one cycle that the model learns through the full training dataset.

The effect of learning rate η and neuron number on the performance of the ANN model I with one hidden layer was first studied. The ANN model with different learning rates $\eta = 0.1, 0.01, 0.001, 0.0001$ and a constant 30 neurons in the single hidden layer was trained. The large learning rates such as $\eta = 0.1, 0.01$ seen in Figure 13 (a), boosted the ANN model and displayed low MSE even at the very beginning of training. However, the MSE maintained the same level until the end of training. By contrast, $\eta =$ 0.001 can reach a low MSE which is similar to the MSE when $\eta = 0.0001$, and converge at an earlier stage. Therefore, $\eta = 0.001$, a commonly used value [30], was selected as the learning rate for the ANN model I. Next, the neuron number was tuned in the single hidden ANN model with the learning rate $\eta = 0.001$. Figure 13 (b) shows that the ANN model with more neurons requires a longer training time. Here we chose 30 neurons in a hidden layer to balance efficiency and accuracy. In the next study, five structures [50], [50,30], [50, 30, 10], [100, 50, 30], [100, 50, 30, 10] with $\eta = 0.001$ were implemented to analyse the effect of interconnection of neurons on the performance of ANN model. A structure indicates the number of hidden layers and the number of neurons in each hidden layer. For example, the second structure [50, 30] means that an ANN model has two hidden layers, the first hidden layer has 50 neurons while the second hidden layer has 30 neurons. It can be observed from Fig. 13 (c) that the second structure is appropriate for ANN model I since it is relatively simple and its MSE converges at a medium rate. The converged MSE in Fig. 13 (c) is smaller than that in Fig. 13 (a) and Fig. 13 (b) by two orders of magnitude, which hints at the importance of a proper structure for an ANN model. Since the converged MSE in Fig. 13 (c) is also much smaller than the $\lambda_{eff}/\lambda_{solid}$ as shown in Fig. 11, the tuned hyperparameters were believed to be a proper combination for ANN model I. Finally, the testing dataset was used to predict $\lambda_{eff}/\lambda_{solid}$ and compared with the 'true' values as shown in Fig. 13 (d). The predicted values have a high correlation (R^2=0.97) with the actual values, indicating that the WCN_{ave} and particle shape characteristics can be used as variables in packing structure models to predict $\lambda_{eff}/\lambda_{solid}$ well.

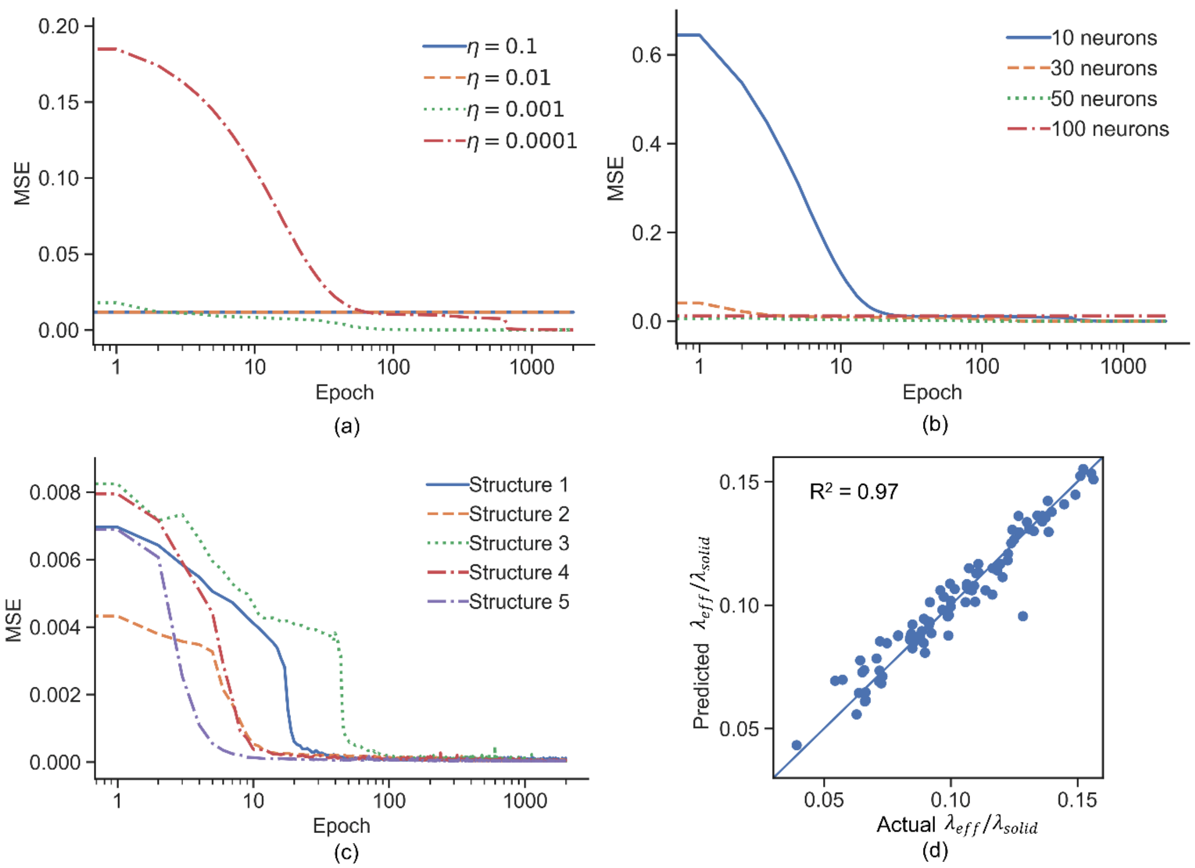

Fig. 13. Tuning learning rate η (a), neuron number in the hidden layer (b) and structure (c) for ANN model I. The correlation between the actual effective thermal conductivity and predicted effective thermal conductivity using the tuned ANN model I on the testing set is show in (d).

4.5.2 *ANN model II: λ_{solid}, sphericity, roundness, WCN_{ave} and porosity as input parameters*

ANN model I considered only microscale and mesoscale parameters. An ANN model II uses a macroscope parameter, porosity, in addition to those. In ANN model I, sphericity and roundness are among the input parameters that describe the geometry of a particle, and capture information from granular materials at particle-scale (microscale). The WCN_{ave} quantifies the particle connectivity and contact quality (mesoscale) but does not quantify the whole sample generally as the bulk properties do at macroscale. Porosity, a bulk property, is used in ANN model II to include a variable at the sample scale (macroscale). Hence, ANN model II involves input parameters across all scales. After using the similar tuning processes for hyperparameters as shown in Fig. 14 (a)-(c), the same structure No.2 [50,30] with learning rate $\eta = 0.001$ were also selected for ANN model II. Figure 14 (d) presents that the R^2 of the relationship between the predicted and actual $\lambda_{eff}/\lambda_{solid}$ is 0.99, which is higher than ANN model I. The porosity as a new input parameter in ANN model II, quantifies the void fraction and loosely indicates the number of particles in a sample. Higher particle counts mean more potential heat transfer pathways in granular assemblies. As explained in previous sections, other parameters also relate to heat transfer mechanisms and capture three diverse aspects: (1) λ_{solid} determines the heat transfer efficiency within particles; (2) sphericity and roundness indicate interparticle contact quality and (3) the WCN_{ave} measures particle connectivity and interparticle contact quality, and also relates to particle diameter (the heat transfer pathway within particles) and thermal conductance. Capturing abundant microstructural information that influence heat transfer certainly results in an accurate λ_{eff} prediction. Consequently, we conclude that considering multiscale microstructural parameters at different scales in λ_{eff} models can result in an accurate λ_{eff} prediction. Supplementary files with the two ANN models (ANN-Model-I.h5 and ANN-Model-II.h5) have been included in this paper for readers to use.

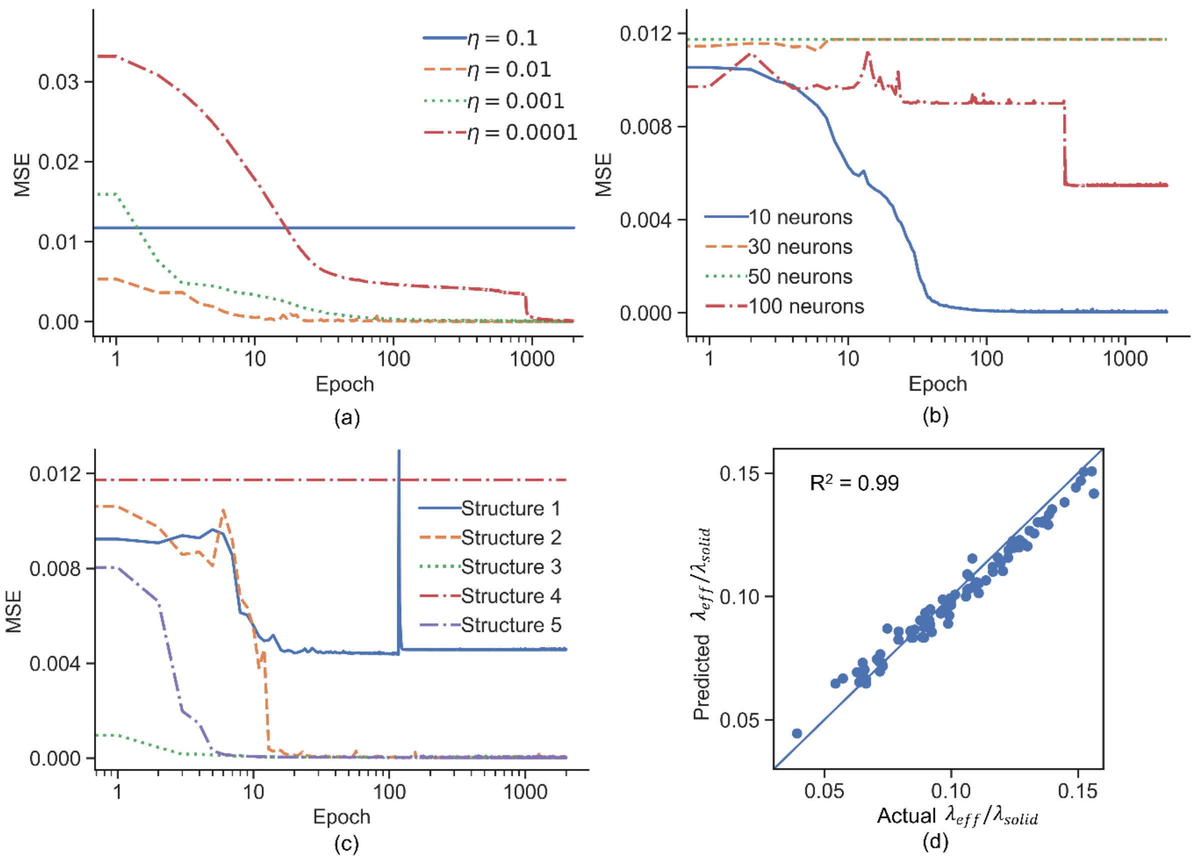

Fig. 14. Tuning learning rate η (a), neuron number in the hidden layer (b) and structure (c) for the ANN model II. The correlation between the actual effective thermal conductivity and predicted effective thermal conductivity using the tuned ANN model II.

5 Conclusions

Microstructure and boundary conditions (e.g., axial loading) in granular materials control λ_{eff}, but microstructural parameters are seldomly used in existing λ_{eff} models, perhaps with the exceptions of (global) porosity and aspect ratio. The advancement of new techniques such as CT, complex network theory, and new numerical simulation methods enable access to the microstructure of natural sands and promote a need for data-driven approaches, for example with the advancement of machine learning techniques, to predict λ_{eff} accurately and efficiently.

Four dry sand assemblies varying in particle size, shape and under different stress levels were CT scanned to achieve image stacks. By applying image processing methods to the image stacks, microstructural parameters such as particle size, 3D sphericity and roundedness and porosity were obtained. In addition, the contact network was constructed to calculate the WCN according to complex network theory. The applicability of these parameters to the ANN model was justified by the analysis of heat transfer mechanism, review of λ_{eff} models and their interplay. The utilisation of microstructural parameters provides the ANN model with some physically-based preconditioning, rather than utilising an ANN model merely as a black-box with somehow random input parameters. Finally, the results indicate that the ANN model, which considers multiple-scale microstructural parameters can predict λ_{eff} well, with best predictions using parameters that characterise granular materials across scales: λ_{solid}, *sphericity, roundness* (at the particle scale), *WCN* (at the mesoscale) and *porosity* (at the macroscale)

This work proves the feasibility of applying ANN to material science, particularly for predictions of λ_{eff}. The physics-based data-driven approach allows the acceleration of material design in a more autonomous and objective process. This paper uses the WCN from a contact network since it is easier to estimate than other mesoscale network features [15]. However, the WCN from the contact network only considers the interparticle contacts but not near-contacts which can be involved in thermal network features [15]. The authors are striving to merge the several aforementioned techniques into a platform which can enable the academic community to achieve microstructural parameters including thermal network features easily and conveniently. Future work includes continuing to increase the current database of granular materials of different shapes and to explore ANN models built with thermal network features and non-dry materials.

Declaration of competing interest

The authors declared that there is no conflict of interest.

Acknowledgements

This research was undertaken in the Imaging and Medical Beam Line (IMBL) at the Australian Synchrotron, Victoria, Australia. The authors would like to acknowledge Dr Anton Maksimenko and the other beam scientists at Australian Synchrotron for their support during our experiments. The authors also thank Dr Tabassom Afshar, Dr Joost van der Linden and Dr Xiuxiu Miao for their support in collecting the CT images and thank Gabrielle E. Abelskamp for proofreading the paper. The first author thanks The University of Melbourne for offering the Melbourne Research Scholarship.

References

[1] C. Pasten, J.C. Santamarina, Thermally induced long-term displacement of thermoactive piles, Journal of Geotechnical and Geoenvironmental Engineering, 140(5) (2014) 06014003.

[2] D.M. Scott, D.K. Das, V. Subbaihaannadurai, V.A. Kamath, A computational scheme for fluid flow and heat transfer analysis in porous media for recovery of oil and gas, Petroleum science and technology, 23(7-8) (2005) 843-862.

[3] W.B. Fei, Q. Li, X.C. Wei, R.R. Song, M. Jing, X.C. Li, Interaction analysis for CO2 geological storage and underground coal mining in Ordos Basin, China, Engineering geology, 196 (2015) 194-209.
[4] M. Moscardini, Y. Gan, S. Pupeschi, M. Kamlah, Discrete element method for effective thermal conductivity of packed pebbles accounting for the Smoluchowski effect, Fusion Engineering and Design, 127 (2018) 192-201.
[5] D.N. Singh, K. Devid, Generalized relationships for estimating soil thermal resistivity, Experimental Thermal and Fluid Science, 22(3) (2000) 133-143.
[6] S. Zhao, J. Zhao, Y. Lai, Multiscale modeling of thermo-mechanical responses of granular materials: A hierarchical continuum–discrete coupling approach, Computer Methods in Applied Mechanics and Engineering, 367 (2020) 113100.
[7] W. Fei, G.A. Narsilio, Network analysis of heat transfer in sands, Computers and Geotechnics (2020).
[8] S. Zhao, J. Zhao, N. Guo, Universality of internal structure characteristics in granular media under shear, Physical Review E, 101(1) (2020) 012906.
[9] W.d. van Antwerpen, C. Du Toit, P. Rousseau, A review of correlations to model the packing structure and effective thermal conductivity in packed beds of mono-sized spherical particles, Nuclear Engineering and design, 240(7) (2010) 1803-1818.
[10] Z. Abdulagatova, I. Abdulagatov, V. Emirov, Effect of temperature and pressure on the thermal conductivity of sandstone, International Journal of Rock Mechanics and Mining Sciences, 46(6) (2009) 1055-1071.
[11] A.M. Abyzov, A.V. Goryunov, F.M. Shakhov, Effective thermal conductivity of disperse materials. I. Compliance of common models with experimental data, International Journal of Heat and Mass Transfer, 67 (2013) 752-767.
[12] R. Askari, S.H. Hejazi, M. Sahimi, Effect of deformation on the thermal conductivity of granular porous media with rough grain surface, Geophysical Research Letters, 44(16) (2017) 8285-8293.
[13] N. Yüksel, The review of some commonly used methods and techniques to measure the thermal conductivity of insulation materials, in: Insulation materials in context of sustainability, IntechOpen, 2016.
[14] R.K. Desu, A.R. Peeketi, R.K. Annabattula, Artificial neural network-based prediction of effective thermal conductivity of a granular bed in a gaseous environment, Computational Particle Mechanics, 6(3) (2019) 503-514.
[15] W. Fei, G.A. Narsilio, J.H. van der Linden, M.M. Disfani, Network analysis of heat transfer in sphere packings, Powder Technology, 362 (2020) 790-804.
[16] L. Papadopoulos, M.A. Porter, K.E. Daniels, D.S. Bassett, Network analysis of particles and grains, Journal of Complex Networks, 6(4) (2018) 485-565.
[17] G.A. Narsilio, J. Kress, T.S. Yun, Characterisation of conduction phenomena in soils at the particle-scale: Finite element analyses in conjunction with synthetic 3D imaging, Computers and Geotechnics, 37(7) (2010) 828-836.
[18] J. Gan, Z. Zhou, A. Yu, Effect of particle shape and size on effective thermal conductivity of packed beds, Powder Technology, 311 (2017) 157-166.
[19] W.-Z. Fang, H. Zhang, L. Chen, W.-Q. Tao, Numerical predictions of thermal conductivities for the silica aerogel and its composites, Applied Thermal Engineering, 115 (2017) 1277-1286.
[20] H. Wei, S. Zhao, Q. Rong, H. Bao, Predicting the effective thermal conductivities of composite materials and porous media by machine learning methods, International Journal of Heat and Mass Transfer, 127 (2018) 908-916.
[21] ASTM D5334-14, Standard Test Method for Determination of Thermal Conductivity of Soil and Soft Rock by Thermal Needle Probe Procedure, in, ASTM International, West Conshohocken, PA, 2014.
[22] S. Ju, J. Shiomi, Materials Informatics for Heat Transfer: Recent Progresses and Perspectives, Nanoscale and Microscale Thermophysical Engineering, 23(2) (2019) 157-172.
[23] E.J. Kautz, A.R. Hagen, J.M. Johns, D.E. Burkes, A machine learning approach to thermal conductivity modeling: A case study on irradiated uranium-molybdenum nuclear fuels, Computational Materials Science, 161 (2019) 107-118.

[24] N. Zhang, H. Zou, L. Zhang, A.J. Puppala, S. Liu, G.J.I.J.o.T.S. Cai, A unified soil thermal conductivity model based on artificial neural network, 155 (2020) 106414.
[25] H. Wei, H. Bao, X. Ruan, Machine learning prediction of thermal transport in porous media with physics-based descriptors, International Journal of Heat and Mass Transfer, 160 (2020) 120176.
[26] B. Yan, R. Gao, P. Liu, P. Zhang, L. Cheng, Optimization of thermal conductivity of UO2–Mo composite with continuous Mo channel based on finite element method and machine learning, International Journal of Heat and Mass Transfer, 159 (2020) 120067.
[27] W. Fei, G.A. Narsilio, J.H. van der Linden, M.M. Disfani, Quantifying the impact of rigid interparticle structures on heat transfer in granular materials using networks, International Journal of Heat and Mass Transfer, 143 (2019) 118514.
[28] J.H. van der Linden, G.A. Narsillio, T. Antoinette, Thermal conductance network model for computerised tomography images of real geomaterials (Conditionally accepted), Computers and Geotechnics, (2019).
[29] M. Wiebicke, E. Andò, I. Herle, G. Viggiani, On the metrology of interparticle contacts in sand from x-ray tomography images, Measurement Science and Technology, 28(12) (2017) 124007.
[30] A. Géron, Hands-On Machine Learning with Scikit-Learn, Keras, and TensorFlow: Concepts, Tools, and Techniques to Build Intelligent Systems, O'Reilly Media, 2019.
[31] B. Mwangi, T.S. Tian, J.C.J.N. Soares, A review of feature reduction techniques in neuroimaging, 12(2) (2014) 229-244.
[32] T.S. Yun, J.C. Santamarina, Fundamental study of thermal conduction in dry soils, Granular matter, 10(3) (2008) 197-207.
[33] W. Fei, G.A. Narsilio, M.M. Disfani, Impact of three-dimensional sphericity and roundness on heat transfer in granular materials, Powder Technology, 355 (2019) 770-781.
[34] H. Shin, J. Santamarina, Role of particle angularity on the mechanical behavior of granular mixtures, Journal of Geotechnical and Geoenvironmental Engineering, 139(2) (2013) 353-355.
[35] P. Zehner, E.U. Schlunder, Thermal Conductivity of Granular Materials at Moderate Temperatures, Chemie. Ingr-Tech., 42 (1970) 933-941.
[36] H. Fricke, A mathematical treatment of the electric conductivity and capacity of disperse systems I. The electric conductivity of a suspension of homogeneous spheroids, Physical Review, 24(5) (1924) 575.
[37] T. Keller, U. Motschmann, L. Engelhard, Modelling the poroelasticity of rocks and ice, Geophysical prospecting, 47(4) (2001) 509-526.
[38] N. Otsu, A threshold selection method from gray-level histograms, IEEE transactions on systems, man, and cybernetics, 9(1) (1979) 62-66.
[39] T.S. Yun, T.M. Evans, Three-dimensional random network model for thermal conductivity in particulate materials, Computers and Geotechnics, 37(7) (2010) 991-998.
[40] T.P. Peixoto, The graph-tool python library, figshare, (2014).
[41] M. Shapiro, V. Dudko, V. Royzen, Y. Krichevets, S. Lekhtmakher, V. Grozubinsky, M. Shapira, M. Brill, Characterization of Powder Beds by Thermal Conductivity: Effect of Gas Pressure on the Thermal Resistance of Particle Contact Points, Particle & Particle Systems Characterization, 21(4) (2004) 268-275.
[42] R. Bauer, E. Schlunder, Effective radial thermal-conductivity of packings in gas flow, part -ii: Thermal conductivity of packing fraction without gas flow, International Chemical Engineering, 18(2) (1978) 189-204.
[43] R. Askari, S. Taheri, S.H. Hejazi, Thermal conductivity of granular porous media: A pore scale modeling approach, AIP Advances, 5(9) (2015).
[44] J.T. Gostick, Versatile and efficient pore network extraction method using marker-based watershed segmentation, Physical Review E, 96(2) (2017) 023307.
[45] J. Sundberg, P.-E. Back, L.O. Ericsson, J. Wrafter, Estimation of thermal conductivity and its spatial variability in igneous rocks from in situ density logging, International Journal of Rock Mechanics and Mining Sciences, 46(6) (2009) 1023-1028.
[46] J. Mo, H. Ban, Measurements and theoretical modeling of effective thermal conductivity of particle beds under compression in air and vacuum, Case studies in thermal engineering, 10 (2017) 423-433.
[47] J. Finney, Random packings and the structure of simple liquids. I. The geometry of random close packing, Proc. R. Soc. Lond. A, 319(1539) (1970) 479-493.

[48] W. Siu, S.-K. Lee, Effective conductivity computation of a packed bed using constriction resistance and contact angle effects, International journal of heat and mass transfer, 43(21) (2000) 3917-3924.
[49] W. Dai, D. Hanaor, Y. Gan, The effects of packing structure on the effective thermal conductivity of granular media: A grain scale investigation, International Journal of Thermal Sciences, 142 (2019) 266-279.

List of figures

Fig. 1. Selected micro-CT slide images of four sands. Images show the variations in particle shape.

Fig. 2. Overview of key steps in image processing to identify individual particles

Fig. 3. Contact network construction for a sample (detailed from the dashed rectangle in Fig. 2 (c))

Fig. 4. CT image of two spheres with a voxel gap. This image displays some partially filled voxels (a) incorrectly identified as contact areas after (b) threshold segmentation.

Fig. 5. Thermal network construction. Red edges represent interparticle contacts while blue edges indicate near-contacts. An equivalent particle cylinder (dark green), an interparticle contact cylinder (orange) and a series of near-contact cylinders (light blue) are used to calculate thermal conductance through the particle, interparticle contact and near-contact. The process is repeated for all particles within the granular material.

Fig. 6. The effective thermal conductivity computed from TCNM and validated by the experimental results of glass beads (GB-L), Ottawa sand (OS), angular sand (AS-L) and crushed schist sand (CS-M).

Fig. 7. The relationship between effective thermal conductivity and (a) WCN_{ave}, (b) porosity, (c) WCN_{ave} and particle shape, and (d) porosity and particle shape. (Click here to access the interactive graphs).

Fig. 8. Variation of (a) effective thermal conductivity, (b) WCN_{ave} , (c) average intercontact area and (d) average coordination number with axial stress (and zero lateral strain).

Fig. 9. The dependence of WCN on equivalent particle diameter for three selected sands

Fig. 10. The relationship between the total heat flux and WCN of particles at inlet and outlet in three selected sands

Fig. 11. The database used to construct the ANN model.

Fig. 12. A heatmap presents the R^2 between each pair of features used in ANN model I

Fig. 13. Tuning learning rate η (a), neuron number in the hidden layer (b) and structure (c) for ANN model I. The correlation between the actual effective thermal conductivity and predicted effective thermal conductivity using the tuned ANN model I on the testing set is show in (d).

Fig. 14. Tuning learning rate η (a), neuron number in the hidden layer (b) and structure (c) for the ANN model Ⅱ. The correlation between the actual effective thermal conductivity and predicted effective thermal conductivity using the tuned ANN model Ⅱ.

List of tables

Table 1 Summary of effective thermal conductivity models that consider particle/pore shape

Table 2 Particle size and axial compression stresses applied to each sample